PCCP

ROYAL SOCIETY OF CHEMISTRY

PAPER

Check for updates

Cite this: *Phys. Chem. Chem. Phys.*, 2021, **23**, 16635

α-Synuclein conformations followed by vibrational optical activity. Simulation and understanding of the spectra†

Andrii Kurochka,[ab] Jiří Průša,[ab] Jiří Kessler,[a] Josef Kapitán[c] and Petr Bouř*[a]

Received 8th June 2021,
Accepted 9th July 2021

DOI: 10.1039/d1cp02574k

rsc.li/pccp

α-Synuclein is a neuronal protein which adopts multiple conformations. These can be conveniently studied by the spectroscopy of vibrational optical activity (VOA). However, the interpretation of VOA spectra based on quantum-chemical simulations is difficult. To overcome the hampering of the computations by the protein size, we used the Cartesian tensor transfer technique to investigate links between the spectral shapes and protein structure. Vibrational circular dichroism (VCD) and Raman optical activity (ROA) spectra of α-synuclein in disordered, α-helical and β-sheet (fibril) forms were measured and analyzed on the basis of molecular dynamics and density functional theory computations. For the disordered and α-helical conformers, a high fidelity of the simulated spectra with a reasonable computational cost was achieved. Most experimental spectral features could be assigned to the structure. So far unreported ROA marker bands of the secondary structure were found for the lower-frequency and CH stretching vibrations. Fibril VCD spectra were simulated with a rigid periodic model of the geometry and the results are consistent with previous studies based on cryogenic electron microscopy. The fibrils also give a specific ROA signal, but unlike VCD it is currently not fully explicable by the simulations. In connection with the computational modeling the VOA spectroscopy thus appears as an extremely useful tool for monitoring α-synuclein and other proteins in solutions.

Introduction

Conformations of α-synuclein (αSyn) are essential for its biological activity. The "native" form is disordered and presumably important for regulation of growth of neurons and their synaptic vesicles.[1] When αSyn binds to lipid membranes, parts of the protein adopt an α-helical conformation, both in *in vitro* and in *in vivo* experiments.[2,3] Most of the research targeting αSyn has been stimulated by its presumably negative role in the development of Parkinson's disease. This illness is characterized by the presence of Lewy bodies, aggregates found in the brain, mostly formed by an insoluble β-sheet-based αSyn form.[4] *In vitro*, αSyn β-sheets organize into many types of amyloidal fibrils,[5,6] and the fine structure of the fibrils determines their toxicity.[7]

Following the protein structural changes in solutions is difficult, and vibrational optical activity (VOA) provides one of a few means suitable for this task.[8] VOA traditionally comprises vibrational circular dichroism (VCD) and Raman optical activity (ROA) measuring differences in absorption (VCD) and scattering (ROA) of left- and right-circularly polarized light. VOA research in the realm of peptides and proteins led to many discoveries, such as the identification of the polyproline II (PPII) secondary structure in the so called disordered or random states,[9] determination of valinomycin conformers in various solvents,[10] and relation of an enhanced VCD signal to the formation and structure of protein amyloidal fibrils.[11] In this context, αSyn represents a convenient benchmark, where the performance of VOA and computational methods needed for interpretation of peptide and protein spectra can be assessed.

Previously, ROA was used to follow αSyn conformational changes, and the disordered structure could be related to the PPII helix.[12] Later, it was shown that Raman and ROA spectroscopies can not only detect transitions from the disordered to α-helical or β-sheet forms, but also differentiate between various α-helical subforms.[13] Using VCD, it was found that interactions with other molecules ("crowding agents") make αSyn fibrils more compact, and the VCD signal and the VCD to

[a] *Institute of Organic Chemistry and Biochemistry, Academy of Sciences, Flemingovo náměstí 2, 16610 Prague, Czech Republic. E-mail: bour@uochb.cas.cz*
[b] *Department of Analytical Chemistry, University of Chemistry and Technology, Technická 5, 16628 Prague, Czech Republic*
[c] *Department of Optics, Palacký University Olomouc, 17. Listopadu 12, 77146, Olomouc, Czech Republic*

† Electronic supplementary information (ESI) available. See DOI: 10.1039/d1cp02574k

absorption ratio become enhanced.[14] It was concluded that the technique is also sensitive to the length and the higher-order morphology of the fibrils. In another study, VCD was used to study parallel β-sheet fibrillar aggregates of an αSyn fragment with lipids.[15] The structure handedness of some amyloid peptides has been shown to depend on the peptide-to-lipid ratio. Such modulation of the αSyn secondary structure through interaction with lipids has been confirmed by other studies and seems to be characteristic of other amyloidogenic proteins as well.[16] VCD was also used to study strongly twisted β-sheets in fibrils of terminal truncated αSyn.[17]

It is thus desirable to link fine VOA spectral features to structural details in the protein more directly. Early on, such predictions were based on learning algorithms and spectra of proteins of known X-ray geometry.[18,19] Simplified models such as the coupled oscillator[20] for VCD and the two-group model[21] for ROA were of limited applicability. Rigorous quantum chemical algorithms became available for small molecules; they are based on the magnetic field perturbation[22] (MFP, for VCD) and response[23] (for both ROA and VCD) theories, and were implemented within the framework of efficient and relatively accurate density functional theory (DFT).[24,25] However, direct applications to large proteins remain problematic because of the extensive computer time and memory needed. Only some spectral features could be understood on smaller molecular models, exploring the locality of important vibrational interactions.[26] Later, VOA spectra of medium-sized peptides and proteins could be calculated directly.[27,28] Computational partitioning techniques, such as molecules-in-molecules[29] and ONIOM,[30] made the accurate computational techniques applicable to even larger systems.

In the present study we use the Cartesian coordinate transfer (CCT) method,[31,32] where vibrational property tensors (force field, dipole and polarizability derivatives) are calculated for arbitrary fragments of the protein and transferred back onto the big molecule. The CCT methodology allows one to use relatively high computational levels, and the accuracy can be tuned by the choice of fragment size.[32,33] In the past, such computations provided very faithful reproduction of VCD[34] and ROA[35] experiments for rigid proteins. For disordered and α-helical αSyn, the CCT method could be combined with molecular dynamics (MD), when the tensors calculated for one structure are transferred onto similar geometries. For fibrils, even the simplified CCT methodology leads to diagonalizations of large matrices that are not possible to perform in a reasonable time. In this case, we therefore used periodic structures of the fibrils to develop a model that could be used for spectral simulation and interpretation.

Methods

Expression of the protein

Following our previous work,[16] competent Escherichia coli cells (BL-21 DE3) were transformed with the pT7-7-SNCA plasmid by a heat shock transformation technique, on a Petri dish inoculated into solid Luria–Bertani (LB) medium and 100 μM ampicillin, and left overnight at 37°. A single colony was picked and inoculated into liquid LB medium with 100 μM ampicillin at 37 °C under constant shaking (220 rpm). Expression was induced by adding isopropyl β-D-1-thiogalactopyranoside (IPTG) to the final concentration of 1 mM when the optical density at 600 nm (OD_{600}) was about 0.5. The cells were harvested 4 h after the induction by centrifugation at 4000*g*, and the centrifuged pellet was resuspended in 10 mM Tris–HCl buffer of pH 7.4 with 1 mM phenylmethanesulfonyl fluoride and 1 mM EDTA. The cells were lysed by 15 min sonication; their DNA was precipitated by adding streptomycin sulfate to a final concentration of 1% and centrifuged for 30 min at 13 500*g*. The supernatant was collected and ammonium sulfate added to 0.3 g mL^{-1}, which led to precipitation of the protein. The precipitate was collected by 20 min centrifugation at 13 500*g*, dissolved in 10 mM Tris–HCl, pH 7.4, and dialyzed against the same buffer for 12 h at 4 °C to remove leftovers of ammonium sulfate. The protein solution was heated to 95 °C for 15 min and cooled down, and unwanted proteins were centrifuged for 20 min at 13 500*g*. The resulting αSyn extract was purified by anion exchange FPLC in a linear gradient of NaCl (0–800 mM) in 10 mM Tris–HCl pH 7.4. Fractions containing αSyn were pooled and concentrated to 200 μM and the solution was dialyzed against 10 mM Tris–HCl pH 7.4 buffer at 4 °C. The purity was confirmed by SDS-PAGE. Aliquots of 1 mL were stored at −20 °C. The protein concentration was measured using tyrosine absorption at 275 nm using ε = 6000 M^{-1} cm^{-1}. A solution of αSyn 200 μM (2.85 mg mL^{-1}) was lyophilized for 24 hours.

Preparation of αSyn conformations

Disordered αSyn and α-helical αSyn were obtained by dissolving 3 mg of dry αSyn in 100 μL 100 mM Tris–HCl buffer with 10 mM NaOH (pH 9). In the presence of sodium dodecyl sulfate (SDS) micelles part of the protein adopts an α-helical conformation.[36] Therefore, SDS was added to the buffer for the α-helical experiments; final concentration of SDS was 400 mM. H_2O solutions were used in Raman/ROA experiments, and D_2O was used for IR/VCD. Before the measurements, the samples were centrifuged to remove occasional solid particles.

αSyn fibrils were prepared by a slow incubation.[16,37] 3 mg αSyn was dissolved in 1 mL of buffer with 10 mM Tris–HCl (pH 7.4), 140 mM NaCl, 0.1 mM EDTA, and 10 mM NaN_3. The solution was put in a microtube, sealed, and incubated for 5 days at 37 °C under 200 rpm shaking. Fibril formation was confirmed by thioflavin T fluorescence. Mature αSyn fibrils were harvested by centrifugation at 14 000*g* for 15 min, when about 100 μL of a gel-like pellet was formed. As for the monomeric forms, IR/VCD experiments were done using D_2O as a solvent. For Raman/ROA measurements, the fibrils were sonicated so that they can be transferred to the measurement cell.

Spectral measurement

IR and VCD spectra were measured with a BioTools ChiralIR-2X instrument using a CaF_2 cell of 50 μm path length, 12 hour accumulation time, and 8 cm^{-1} resolution. Spectra of the solvents were subtracted as a baseline. Backscattered Raman

 This journal is © the Owner Societies 2021

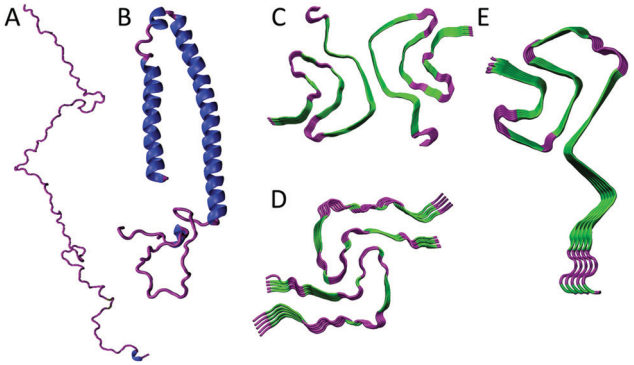

Fig. 1 αSyn conformations: (A) Random coil (MD snapshot based on PPII). (B) α-helix (MD structure based on the 1XQ8 micelle-bond structure[36]) and β-sheets/fibrils 6CU7[5] (C), 6CU8[5] (D) and 2NA0[40] (E). Geometries of B–E were downloaded from https://www.rcsb.org/.

and scattered circular polarization (SCP)[38] ROA spectra were measured on a custom-made spectrometer (PU, Olomouc),[39] using 532 nm laser excitation, 340–550 mW laser power at the sample, and 18–30 h acquisition times. For a control, some ROA and Raman spectra of fibrils were re-measured on a commercial BioTools ChiralRaman-2X spectrometer using similar conditions. These spectra were similar, but with lower signal to noise ratio, and are not shown. The spectrum of the solvent was subtracted from the Raman spectra.

Molecular dynamics and density functional theory

Monomer αSyn molecules in the standard polyproline II[41] or partial α-helical[36] conformation (Fig. 1) were placed in a box ($450 \times 30 \times 30$ or $150 \times 80 \times 80$ Å^3, respectively) otherwise filled with water and sodium counterions. Short MD runs were performed to partially relax these canonical structures. The system was minimized and subjected to a short (0.4 ns) equilibration, and in a 1 ns production run 1000 geometry snapshots were produced, separated by 1 ps. The Amber8 program,[42] 1 fs integration time, *NVT* ensemble and 300 K temperature were used. Amber99[43] and TIP3P[44] force fields were chosen for the protein and water, respectively.

A randomly selected snapshot (without water) was subjected to further DFT calculations. Using the CCT method,[31,32,35] the αSyn molecule in the snapshot was divided into 4-amide overlapping fragments with one-amide increment sliding along the protein chain, and the fragments were partially optimized using the normal mode vibrational coordinates[45] and 100 cm^{-1} frequency limit.[46] Then atomic property tensors – second energy, first dipole and polarizability derivatives – were calculated and transferred back to the selected and other 999 snapshots. The effect of the averaging is shown in Fig. S1 (ESI†) for ROA of the disordered form: the individual snapshot provides already the main spectral features, and the average becomes more realistic. Program QGrad[43,45] was used for the normal mode optimization[45,47] and Gaussian[48] was used for the quantum chemistry performed at the B3PW91/[49]6-31++G**/CPCM[50](H_2O) approximation level. For the α-helix potentially requiring longer-distance interactions,[32,33] longer 7-amide fragments and a 6-31G** basis set were tried as well, which, however, did not lead to better results.

The intensity of a ground to excited state transition is determined by the electric $\langle G|\mu|E\rangle$ and magnetic $\langle G|m|E\rangle$ transition dipole moments, and electric $\langle G|\alpha|E\rangle$, magnetic $\langle G|G'|E\rangle$ and quadrupole $\langle G|A|E\rangle$ transition polarizabilities.[51] In particular, the IR and VCD band areas are proportional to the dipole D and rotational R strengths, whereas the backscattered Raman (I_{Ram}) and SCP ROA (I_{ROA}) intensities require analogous isotropic invariants.[22,38]

$$D = \mu_\alpha \mu_\alpha \tag{1}$$

$$R = \mathrm{Im}(\mu_\alpha m_\alpha) \tag{2}$$

$$I_{\mathrm{Ram}} = K(\alpha_{\alpha\alpha}\alpha_{\beta\beta} + 7\alpha_{\alpha\beta}\alpha_{\alpha\beta}) \tag{3}$$

$$I_{\mathrm{ROA}} = \frac{8K}{v}\left(3\alpha_{\alpha\beta}G'_{\beta\alpha} - \alpha_{\alpha\alpha}G'_{\beta\beta} + \frac{\omega}{3}\varepsilon_{\alpha\beta\gamma}\alpha_{\alpha\varepsilon}A_{\beta\gamma\varepsilon}\right) \tag{4}$$

where for brevity we omitted the states, so that $\mu = \langle G|\mu|E\rangle$, *etc.*, K is a constant, v is the velocity of light, and ω is the angular frequency, the Einstein summation convention is used, and ε is the antisymmetric tensor. Smooth spectra were plotted using Lorentzian bands of 10 cm^{-1} full widths at half height.

Spectra of αSyn fibrils were simulated for rigid geometries only. Three fibril types (6CU7,[5] 6CU8[5] and 2NA0,[40] Fig. 1) were selected from the protein database (https://www.rcsb.org/), all formed by parallel protein strands in the β-sheet conformation. Two adjacent αSyn strands were taken; terminal protein residues not involved in the β-sheet conformation were ignored. As for the monomers, vibrational parameters were calculated using fragments and the CCT method. The fragments contained 8 amide groups, four of each strand, so that the strand–strand H-bond interactions were included. Only a smaller 6-31G** basis set could be used in this case; therefore the ROA polarizabilities more dependent on the basis set were calculated separately using the 6-31++G** basis set and 4 amide fragments. The CCT fragmentation is illustrated in Fig. S2 (ESI†). These calculations were extended to longer periodic geometries as detailed below.

Amide I frequency scaling

Special attention has been paid to C=O bond stretching. This mode is essential for IR and VCD spectral interpretation, but for multiple reasons it is calculated with a different precision than lower-frequency vibrations.[52,53] Therefore, for each C=O bond, a force constant was calculated from the harmonic force field, scaled by a factor determined from experiment, and projected back onto the original force field.

To achieve this, we write the potential energy as

$$V = \frac{1}{2}\sum_{i=1}^{6} f_i Q_i^2 = \frac{1}{2}\sum_{\beta=1}^{6}\sum_{\alpha=1}^{6} \Delta r_\alpha F_{\alpha\beta} \Delta r_\beta, \tag{5}$$

where r_α are the x, y and z coordinates of the C and O atoms, and f_i and $F_{\alpha\beta}$ are the normal mode and Cartesian force constants. To obtain the local normal mode coordinates Q_i we start from the CO bond length d and define a transformation matrix s for

small changes

$$\Delta d = \sum_{\alpha=1}^{6} s_{\alpha,1}\Delta r_\alpha, \tag{6}$$

where $s_{Cx,1} = (r_{Cx} - r_{Ox})/d$ and $s_{Ox,1} = -s_{Cx,1}$, and analogously for the y and z components. We complete the definition by setting $s_{\alpha,i} = \delta_{\alpha i}$ for $i = 2,\ldots,6$. Next, we orthonormalize columns of s by the Gram–Schmidt procedure, obtaining a new matrix: $S_{\alpha,j} = s'_{\alpha,j} \Big/ \sqrt{\sum_{\alpha=1}^{6} s'^2_{\alpha,j}}$, where $s'_{\alpha,j} = s_{\alpha,j} - \sum_{k=1}^{j-1}\left(\sum_{\beta=1}^{3} s_{\beta,j}S_{\beta,k}\right)S_{\alpha,k}$. In a matrix form the normal modes are related to Cartesian coordinates by

$$Q = S\Delta r, \tag{7}$$

where $S^tS = 1$, and the internal force field is

$$f = SFS^{t}. \tag{8}$$

We associate f_{11} with the C=O force constant, and define the scaled force field as $f'_{11} = c^2 f_{11}$, $f'_{1i} = f'_{i1} = cf_{1i}$ (for $i \neq 1$), $f'_{ij} = f_{ij}$ $(i \neq 1,\ j \neq 1)$, where c is the scaling factor. Finally, the scaled Cartesian force constants were obtained by a back transformation, $F' = S^t f' S$. For amide group COs, we used c = 0.95/0.94, and for carboxyl groups c = 0.96/0.93, depending on the 6-311++G**/6-31** basis set.

Fibril periodic model

By the CCT approach it is possible to model systems up to $\sim$−10 000 atoms.[35] This is not sufficient for longer fibrils. We therefore treat them as ideal one-dimensional periodic structures, as done for crystals.[54] The vibrational Hamiltonian within the harmonic approximation is

$$H = \frac{1}{2}\sum_{J}\sum_{\lambda\in J} m_\lambda \Delta\dot{r}_\lambda^{(J)^*}\Delta\dot{r}_\lambda^{(J)} + \frac{1}{2}\sum_{J'}\sum_{J}\sum_{\lambda\in J'}\sum_{\mu\in J}\Delta r_\lambda^{(J')^*}F_{\lambda\mu}\Delta r_\mu^{(J)}, \tag{9}$$

where m_λ are atomic masses and $\Delta r_\lambda^{(J)}$ are deviations from equilibrium positions in elementary cell J. We suppose that a fibril contains N such cells, where N is a large number. As usual for crystals,[55] we make a Fourier-like transformation

$$\Delta r_\lambda^{(J)} = \frac{1}{\sqrt{N}}\sum_{q=0}^{N-1}\exp\left(\frac{2\pi qJ}{N}i\right)R_\lambda \tag{10}$$

where $i = \sqrt{-1}$, and R_λ are deviations in a reference cell. Eqn (9) becomes

$$H = \frac{1}{2N}\sum_{J}\sum_{q}\sum_{q'}\left[\exp\left(\frac{2\pi(q-q')J}{N}i\right)\sum_{\lambda} m_\lambda \dot{R}_\lambda^{*}\dot{R}_\lambda + \sum_{J'}\sum_{\lambda}\sum_{\mu} R_\lambda^{*}F_{\lambda\mu}R_\mu \exp\left(2\pi\frac{qJ - q'J'}{N}i\right)\right]. \tag{11}$$

Next, we use the orthonormality of the plane waves, $\frac{1}{N}\sum_{J}\exp\left(\frac{2\pi(q-q')J}{N}i\right) = \delta_{qq'}$, where δ is the Kronecker delta, the periodicity of F, $F_{\lambda\in J',\mu\in J} = F_{\lambda\in 0,\mu\in J-J'}$, and define the dynamic matrix

$$D_{\lambda\mu}^{q} = F_{\lambda\in 0,\mu\in J}\sum_{J}\exp\left(\frac{2\pi qJ}{N}i\right) \tag{12}$$

so that

$$H = \frac{1}{2}\sum_{q}\left(\sum_{\lambda} m_\lambda \dot{R}_\lambda^{*}\dot{R}_\lambda + \sum_{\lambda}\sum_{\mu} R_\lambda^{*}D_{\lambda\mu}^{q}R_\mu\right). \tag{13}$$

Next, we introduce normal mode vibrational coordinates Q_J,

$$\sqrt{m_\lambda}R_\lambda = \sum_{I} S_{\lambda I}Q_I \tag{14}$$

where $S^*S^t = 1$, and $\sum_{\lambda}\sum_{\mu} S_{\lambda I'}^{*}\frac{D_{\lambda\mu}^{q}}{\sqrt{m_\lambda m_\mu}}S_{\mu I} = \delta_{II'}\omega_I{}^2$. The Hamiltonian simplifies to

$$H = \frac{1}{2}\sum_{q}\sum_{I}\left(\dot{Q}_I{}^2 + \omega_I{}^2 Q_I{}^2\right), \tag{15}$$

where ω_J is the normal mode frequency, and both Q_I and ω_I depend on q.

Within this model, we get the vibrational frequencies by diagonalizing N matrices D^q, each of a dimension $(3Nat/N)$, for which the computational time roughly scales as $N \times (3Nat/N)^3$, where Nat is the number of atoms in the fibril. This is much faster than a direct diagonalization of the force field F, scaling as $(3Nat)^3$. For example, for N = 20, the speed-up factor is N^2 = 400.

For computations of transition intensities we realize that the Hamiltonian wavefunction in eqn (15) is a product of harmonic oscillator wavefunctions, $\psi = \prod_q\prod_I \psi_{qI}$. It is convenient to introduce helical coordinates, replacing $(\mu_x,\ \mu_y,\ \mu_z)$ by $(\tilde{\mu}_{-1} = \frac{\mu_x - i\mu_y}{\sqrt{2}},\ \tilde{\mu}_0 = \mu_z,\ \tilde{\mu}_1 = \frac{\mu_x + i\mu_y}{\sqrt{2}})$, *etc.* We suppose that the fibril propagates along z, and neighboring cells (αSyn strands) twist by angle τ. Then helical coordinates in cell J differ from those in the 0th reference cell by a phase factor only, $\tilde{\mu}_k(J) = e^{ikJ\tau}\tilde{\mu}_k(0)$. Different phases of the vibrational motion in various cells are given by eqn (10). For a fundamental transition we get the transition dipole moment as

$$\tilde{\mu}_k = \sum_{J}\frac{\partial\tilde{\mu}_k(J)}{\partial Q_I}\langle 0|Q_I|1\rangle = \frac{\partial\tilde{\mu}_k(0)}{\partial Q_I}s_{1,k}\sqrt{\frac{\hbar}{2\omega_I}} \tag{16}$$

where $\hbar$ is the Planck constant, $s_{1,k} = \frac{1}{\sqrt{N}}\sum_{J=0}^{N-1} e^{i\xi_k J} = \frac{1}{\sqrt{N}}\frac{e^{i\xi_k N} - 1}{e^{i\xi_k} - 1}$, and $\xi_k = \frac{2\pi q}{N} + k\tau$. Normal mode derivatives can be calculated from the Cartesian ones, $\frac{\partial\tilde{\mu}_k(0)}{\partial Q_I} = \sum_{\lambda}\frac{\partial\tilde{\mu}_k(0)}{\partial R_\lambda}\frac{S_{\lambda I}}{\sqrt{m_\lambda}}$. The expression for the transition polarizability α is analogous,

$$\tilde{\alpha}_{ij} = \frac{\partial\tilde{\alpha}_{ij}(0)}{\partial Q_I}s_{1,i+j}\sqrt{\frac{\hbar}{2\omega_I}} \tag{17}$$

For m, G' and A, additional terms arise from the origin dependence, $\tilde{m}_k = i\varepsilon_{-klm}\tilde{R}_l\dot{\tilde{\mu}}_m$, $\tilde{G}'_{ij} = -\frac{i\omega}{2}\varepsilon_{-jkl}\tilde{R}_k\tilde{\alpha}_{il}$, and

This journal is © the Owner Societies 2021

$\tilde{A}_{ijk} = -\delta_{j,-k}\tilde{R}_l\tilde{\alpha}_{il} + \frac{3}{2}(\tilde{R}_j\tilde{\alpha}_{ik} + \tilde{R}_k\tilde{\alpha}_{ij})$, where for cell J the shift is $\tilde{R}_l(J) = LJ\delta_{l0}$, where L is the z-size (length) of the elementary cell. We can suppose that these terms dominate in the fibril optical activity, and neglect the intrinsic ones.[56,57] Then

$$\tilde{m}_k = ikL\frac{\partial\tilde{\mu}_k^q}{\partial Q_I}s_{2,k}\sqrt{\frac{\hbar\omega_I}{2}}, \quad (18)$$

$$\tilde{G}'_{ik} = -\frac{ik\omega L}{2}\frac{\partial\tilde{\alpha}_{ik}(0)}{\partial Q_I}s_{2,i+k}\sqrt{\frac{\hbar}{2\omega_I}} \quad (19)$$

$$\tilde{A}_{ijk} = \left[-\delta_{j-k}L\tilde{\alpha}_{i0}^{\lambda\varepsilon}s_{2,i} + \frac{3}{2}L\left(\delta_{j0}\frac{\partial\tilde{\alpha}_{ik}(0)}{\partial Q_I}s_{2,i+k} + \delta_{k0}\frac{\partial\tilde{\alpha}_{ij}(0)}{\partial Q_I}s_{2,i+j}\right)\right] \times \sqrt{\frac{\hbar}{2\omega_I}} \quad (20)$$

where $s_{2,k} = \frac{1}{\sqrt{N}}\sum_J Je^{i\xi_k J} = \frac{(N-1)e^{i\xi_k(N+1)} - Ne^{i\xi_k N} + e^{i\xi_k}}{\sqrt{N}(e^{i\xi_k}-1)^2}$.

The αSyn monomer unit was propagated with different twists ($\tau = -2^\circ,\ldots,2^\circ$) and lengths ($N = 1,\ldots,380$), the dynamic matrix (eqn (12)) contained monomer–monomer interactions obtained by the DFT and CCT methods for the dimer, and longer-distance terms were approximated by the dipole–dipole interactions, with an effective relative permittivity $\varepsilon_r = 3$.[34,58]

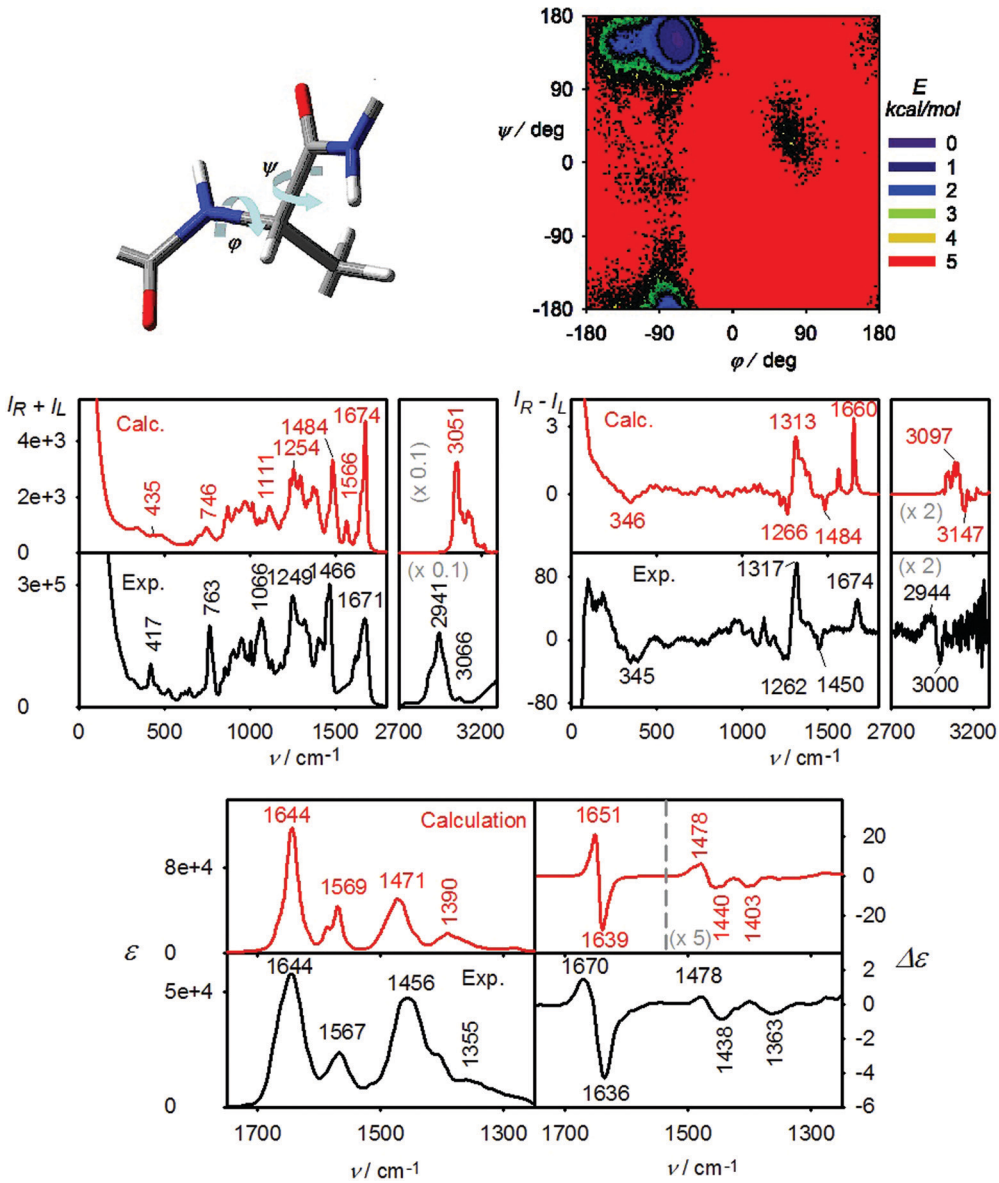

Fig. 2 Disordered αSyn: MD (φ, ψ) angle distribution converted to free energy, and calculated and experimental Raman ($I_R + I_L$), ROA ($I_R - I_L$), IR (ε) and VCD ($\Delta\varepsilon$) spectra. The IR and VCD spectra were measured in D_2O, and the calculated C═O force constants were changed to fit the experimental data.

Results and discussion

Disordered αSyn has quite distinct Raman and ROA spectra, details of which have been provided previously.[13] This could be convincingly reproduced by simulations (Fig. 2). As follows from the Ramachandran plot (top of the figure), the protein largely remains in the PPII conformation with the (φ, ψ) angles around (-75°, 150°). During the short 1 ns MD run the structure is disrupted only occasionally, and the second most-populated conformation with (φ, ψ) $\sim$ (-135°, -145°) corresponds to the β-sheet form.[41] For simplicity, we use the terms disordered and PPII conformations as synonyms. It is generally accepted that the "random" peptide and protein conformation is to a great extent composed of a PPII left handed helix.[8,9]

Disordered αSyn has a rich Raman spectrum with particularly strong signals from aliphatic and aromatic side chains (ref. 35, Table 1). An aromatic C=C stretching vibration overlaps with the amide I band and is calculated to be rather high (1673 cm^{-1}) compared to the experimental value ($\sim$1616 cm^{-1}), which is mostly attributed to errors stemming from DFT and harmonic approximations. The ROA spectrum contains fewer bands and is dominated by the (experimentally) 1317 cm^{-1} positive $^{\alpha}$CH bending band with a shoulder at 1390 cm^{-1}, which is well reproduced by the calculation (Fig. 2). A negative broader signal around 1262 cm^{-1} also originates in $^{\alpha}$CH bending, mixed with amide III modes (CN stretching and NH bending). This part of the ROA protein spectrum ($\sim$1200–1350 cm^{-1}) has been found to be very dependent on the secondary structure.[35,59] Relatively strong are also the positive amide I band at 1674 cm^{-1} and the negative signal at 1450 cm^{-1}. The latter calculated at 1484 cm^{-1} partially originates from CH_2 scissoring.

The ROA spectrum below 1200 cm^{-1} lacks strong features; resolved bands appear again at the lowest frequencies, starting with the 345 cm^{-1} negative band with contributions of the amide out of plane motion. In the experimental spectrum, two positive strong ROA bands appear at 185 and 97 cm^{-1}, and the signal becomes negative again below 78 cm^{-1}, close to the spectrometer limit at $\sim$50 cm^{-1}. The computations approximately reproduce this trend and suggest that the lowest-frequency optical activity can be linked to delocalized protein backbone modes.

At the other highest frequency end of the spectrum, we see a positive ROA with the experimental maximum at 2944 cm^{-1}. The largely positive signal is approximately reproduced by the computations, which are, however, highly inaccurate in this region because of the anharmonic effects.[39] Above $\sim$3050 cm^{-1} the experimental ROA spectrum is dominated by the noise because of the strong water/buffer scattering.[60]

The experimental IR absorption spectrum shown in the lower part of Fig. 2 is dominated by the amide I′ band (prime for the deuteration) at 1644 cm^{-1}, generating a +(1670 cm^{-1})/−(1636 cm^{-1}) "couplet" in VCD. The single amide I′ IR band and the VCD couplet are characteristic of disordered peptide and protein structures.[8,9,26] The simulated VCD intensity is somewhat larger than the experimental one, presumably because the real structure is less regular than the PPII conformation predicted/imposed by the short-time MD. The 1567 cm^{-1} IR band comes from the C=O stretching of the COO^- side chain groups (αSyn contains 5 aspartate and 18 glutamate residues). These are not chiral and do not much contribute to VCD, where only bands of amide II′ and extended amide III′ vibrations are clearly detectable within 1300–1500 cm^{-1}.

The NMR-based partially α-helical geometry[36] remained reasonably stable during the limited 1 ns MD run, *i.e.* residues 1–84 retained the α-helical conformation, while residues 85–140 at the C end of the peptide chain were disordered, close to the polyproline II conformation. This reflects the Ramachandran plot (Fig. 3, top), where the α-helical angles (φ, ψ) oscillate around $\sim$(-67°,-42°).

Compared to the disordered case (Fig. 2) the α-helical Raman experimental spectrum (Fig. 3) exhibits a few changes. The relative band intensity at 417 cm^{-1} is smaller, a new band appears at 525 cm^{-1} and the intensity is restructured within $\sim$800–1100 cm^{-1}. The higher-frequency 1460 and 1653 cm^{-1} bands are slightly shifted. In some changed bands (525, 926 cm^{-1}) we identified a contribution of amide out of plane deformation and tyrosine vibrations. The intensities within 800–1100 cm^{-1} are not well reproduced by the calculation, which may be attributed to the interaction with SDS micelles, not included in our model.

Bigger changes occur in the ROA spectra. The sharp positive 1317 cm^{-1} PPII band of $^{\alpha}$C–H bending splits into two (1304/1346 cm^{-1}) for the α-helix, whereas the minimum at 1262 cm^{-1} travels down to 1237 cm^{-1}. This is reproduced by the simulations, although the calculated splitting around 1347 cm^{-1} is smaller. The amide I ROA band remains positive, but its position shifts down from 1674 cm^{-1} to 1665 cm^{-1}. As for the disordered form, close to the 50 cm^{-1} instrumental limit, strong ROA appears, such as a minimum at 168 cm^{-1} and maxima at 73 and 125 cm^{-1}. As for disordered αSyn, the signal becomes negative at the lowest frequencies. It crosses zero at $\sim$51 cm^{-1}. These drastic ROA

Table 1 Assignment and positions (cm^{-1}) of selected vibrational bands

Raman/ROA spectra	Calculated	Experimental
ν(C–H)	3050–3170	2853–3000
Amide I, PPII	1674	1671
Amide I, α-helix	1655	1653
Amide I, fibrils	1667	1667
Arom. (ν(C=C))	1673	1616
Amide II	$\sim$1550	$\sim$1555
δ(C–H), CH_2, CH_3	1424–1484	1424–1480
Amide III, δ(C–H), $^{\alpha}$CH	1265–1384	1262–1390
Amide, oop	$\sim$342	$\sim$345
CH_3 wagging, backbone	$\sim$165	$\sim$167
Backbone	$\sim$70–125	$\sim$70–125

IR/VCD spectra, in D_2O	Calculated			Experimental		
	PPII	α-helix	Fibrils[a]	PPII	α-helix	Fibrils
Amide I′	1644	1642	1614–1650	1644	1642	1620–1647
Asp, Glu ν(C=O)[b]	1569	1570	1576	1567	1566	1568
Amide II′, δ(N–D)	1471	1469	1468	1456	1458	1452
Amide III′, δ(C–H)	1390	1386	1345	1355	1342	1348

[a] For the 6CU7 geometry. [b] Out of phase in CO_2^-.

This journal is © the Owner Societies 2021

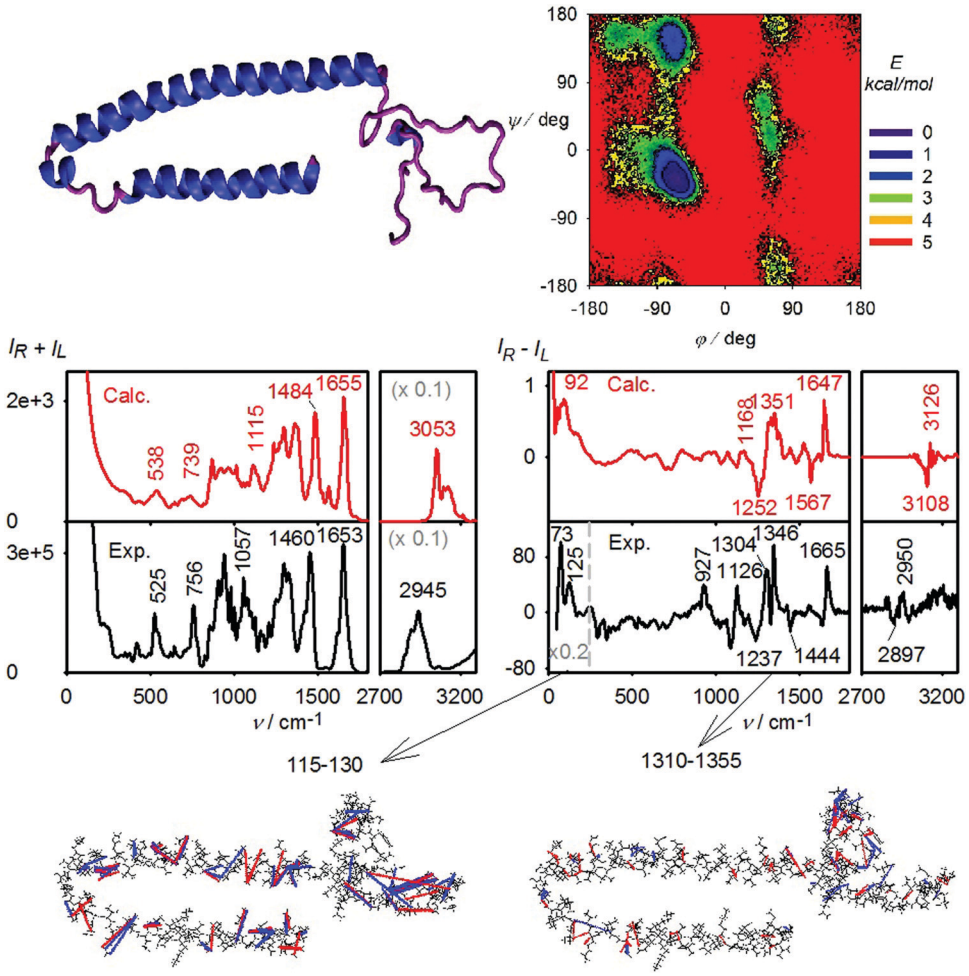

Fig. 3 Partially α-helical αSyn, the (φ, ψ) angle distribution and free energy (top), calculated and experimental Raman ($I_R + I_L$) and ROA ($I_R - I_L$) spectra (middle), and atomic contributions to ROA in the two regions (115–130 cm^{-1}, and 1310–1355 cm^{-1}, bottom). For the contribution plotting, eqn (4) was broken down into two-atomic terms, *e.g.* $\alpha_{\alpha\beta}G'_{\beta\alpha} = \sum_i \frac{\partial\alpha_{\alpha\beta}}{\partial Q_i}\frac{\partial G'_{\beta\alpha}}{\partial Q_i} = \sum_\lambda \sum_\mu \left(\sum_\gamma \sum_\delta \sum_i \frac{\partial\alpha_{\alpha\beta}}{\partial Q_i}\frac{\partial G'_{\beta\alpha}}{\partial Q_i} S_{\lambda\gamma,i} S_{\mu\delta,i} \right)$, where ($\lambda$,$\mu$) run over all atom pairs, S is the Cartesian-normal mode transformation matrix, γ and δ run over *x*, *y* and *z*, and *i* runs over normal modes Q_i with frequencies in the chosen interval. Negative and positive terms are plotted using blue and red curves connecting the pair atoms.

changes with the secondary structure indicate that the low-frequency measurement may be quite useful for studies of proteins and particularly α-helices. Similar positive/negative bands were seen also in partially α-helical globular proteins, such as bovine α-lactalbumin (64 (+)/168 (−) cm^{-1}) and human serum albumin (67 (+)/168 (−) cm^{-1}).[35] However, a positive band at 64 cm^{-1} was exhibited also by concanavalin A, predominantly formed by β-sheets.[35]

A relatively unexplored is also the ROA of the C–H stretching vibrations. The predominantly positive 2944 cm^{-1} signal of the disordered form dramatically changes for the α-helix, to an alternate four-sign pattern, 2853 (+), 2897 (−), 2950 (+) and 2994 (−) cm^{-1}. As for the disordered form, the experimental spectrum for higher frequencies becomes unreliable because of low CID (ratio of the ROA and Raman signals) and high noise.[60] In particular, the 2853 cm^{-1} band might be affected by a strongly polarized SDS band at this position. The calculations do predict a dramatic difference between the disordered and α-helical αSyn, and the calculated 3108 (−)/3126 (+) cm^{-1} bands are probably connected to the observed 2897/2950 cm^{-1} signals, but as said above they cannot be fully trusted because of the anharmonic effects.

Previous studies suggested that the ROA signal comes almost exquisitely from the protein backbone, while the Raman signal is approximately the sum of contributions from individual protein residues.[35] To single out side chain, aromatic and backbone contributions for αSyn, we deleted polarizability derivatives of relevant atoms in the computations (Fig. S3, ESI†). This shows, for example, that the aromatic residues cause sharp Raman bands calculated at 844, 1013, 1234 and 1670 cm^{-1}. Also, as expected, the side chains usually do not contribute significantly to ROA, except for the lowest-frequency region (<300 cm^{-1}). Here, they make a huge impact, and even a sign flip occurs when their contribution is deleted.

Another insight is provided by the two-atomic contributions to ROA intensities visualized at the bottom of Fig. 3. The intensities

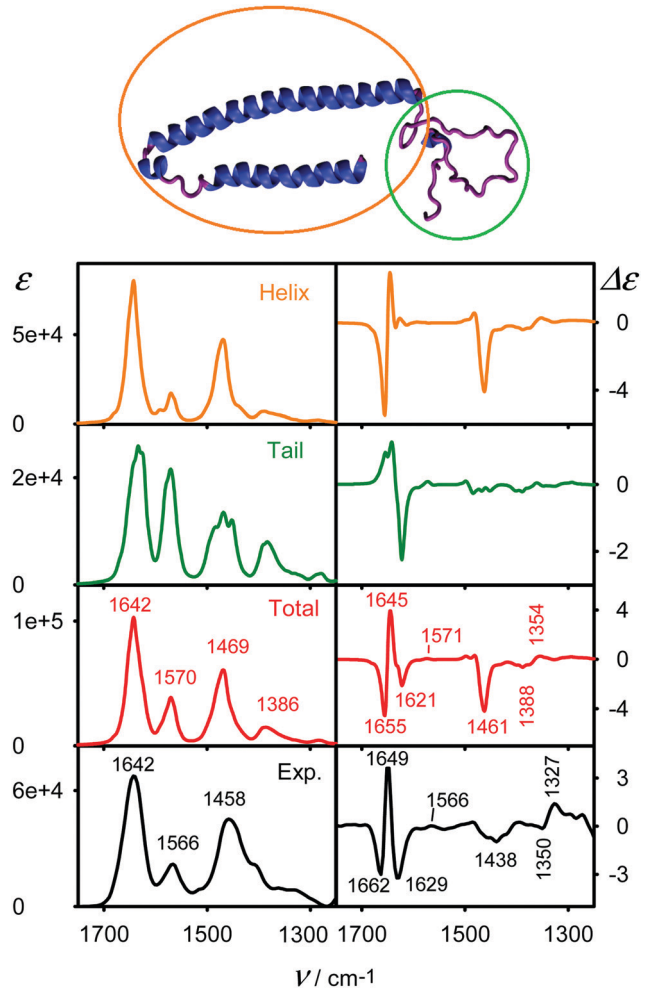

Fig. 4 From top to bottom, α-helical αSyn, and IR and VCD spectra calculated for the purely helical and disordered parts and whole protein, and the experimental spectra (in D_2O). In the calculations, the same snapshots were averaged, using dipole derivatives of atoms from the desired molecular part.

within 115–130 cm^{-1} originate largely on the side chain atoms, as these are moving during the low-frequency backbone vibrations. Higher-frequency modes are more local; for example, the intensity within 1310–1355 cm^{-1} often comes from the $^{\alpha}$C–H bending coupled with amide carbonyl carbons. For this motion it is interesting that coupling with carbon from the neighboring amino acid residue contributes more to ROA than coupling to the carbon immediately attached to $^{\alpha}$C–H. At the $^{\alpha}$C–H bending frequencies 1310–1355 cm^{-1} the side chains contribute, too, but rather in a random way, while the $^{\alpha}$C–H/carbonyl contributions are all positive and prevail on the average.

The simulations indicate that the contribution of the disordered molecular part to the ROA spectrum of the α-helical form is rather minor (Fig. S4, ESI†). In IR and VCD spectra the two molecular parts have more comparable intensities (Fig. 4). Compared to the α-helical part, the 1570 cm^{-1} (calc.) IR band of carboxyl C═O stretching is much stronger for the tail. This reflects the high number of acidic amino acids in the disordered part of the C-terminus (10 glutamates and 5 aspartates out of 43 residues). The α-helical N-terminus contains 8 glutamates and one aspartate only, out of 97.

Although the side chains move relatively freely, the carboxyl C═O stretching seems to cause a weak positive VCD, both in the calculated and experimental spectra. Amide I′ band VCD bands are, of course, much stronger, with a w-shaped (calc. 1655 (−), 1645 (+), 1621 (−) cm^{-1}) dominating the signal of the α-helix. This pattern is largely conserved for the whole protein when the contribution of the tail is added. At 1461 cm^{-1} the calculation correctly predicts a larger intensity of the amide II′ negative VCD band compared to the disordered form (Fig. 2), although this experimental band at 1438 cm^{-1} is much broader than the simulated one. A weaker couplet calculated at 1386 (−)/1354 (+) cm^{-1} reasonably well corresponds to the observed one at 1350 (−)/1327 (+) cm^{-1}.

Finally, the calculated IR and VCD spectra of fibrillated αSyn are compared to the experimental ones in Fig. 5. As expected,[8,61] the amide I′ IR band splits due to the specific coupling of the C═O stretching vibrations in the β-sheet plane.[62] In the experimental spectrum, instead of one band at 1644 (disordered) or 1642 (α-helix) cm^{-1} we see a sharper peak at 1620 cm^{-1} and a shoulder at 1647 cm^{-1}. The experimental intensity of the 1452 cm^{-1} band might be affected by HDO contamination, which was difficult to avoid even when using a closed measurement cell. For VCD, instead of the couplet (disordered) and w-shape (α-helix), amide I′ vibrations provide a negative signal at 1632 cm^{-1}. A smaller positive band appears at 1604 cm^{-1}. It should be said that αSyn fibrils prepared with a "crowding" agent exhibited a different, enhanced VCD signal.[14] In our case, however, the ratio of VCD to IR intensity measured for the maxima in the amide I′ region is small, about 5.4×10^{-5}, close to the values of the α-helical (5.2×10^{-5}) and disordered (-7.7×10^{-5}) forms. A negative amide II′ band appears at 1454 cm^{-1}.

The simulations using the periodic model were done for the three fibril structures obtained from the PDB database. All calculated spectra reasonably well explain the amide I′ splitting in experimental IR. The (calc.) 1614 cm^{-1} signal is polarized along the fibril axis, and normal modes contributing to the 1650 cm^{-1} shoulder are mostly polarized in directions perpendicular to it. The first and third (2NA0 and 6CU7) geometries show a higher-frequency shoulder less intense than those in the experimental spectrum. When part of the disordered spectrum is subtracted from the experimental spectrum the agreement is much better. For VCD, the third structure (6CU7) is seen to be the best match to the experimental one.

However, when interpreting fibril spectra, it must be borne in mind that they depend both on the length and on the twist.[63] In Fig. 6, the IR and VCD spectra of the 6CU7 model are simulated for 60, 90, 180 and 360 αSyn molecules. Apparently, the IR spectra virtually do not change with length, but the VCD slowly converges to a shape reasonably similar to the experimental one. We do not know how the solution fibrils are close to the cryo-EM experiment, where ionic liquids were present as crystal enhancing additives.[5] Nevertheless, the geometry seems

 This journal is © the Owner Societies 2021

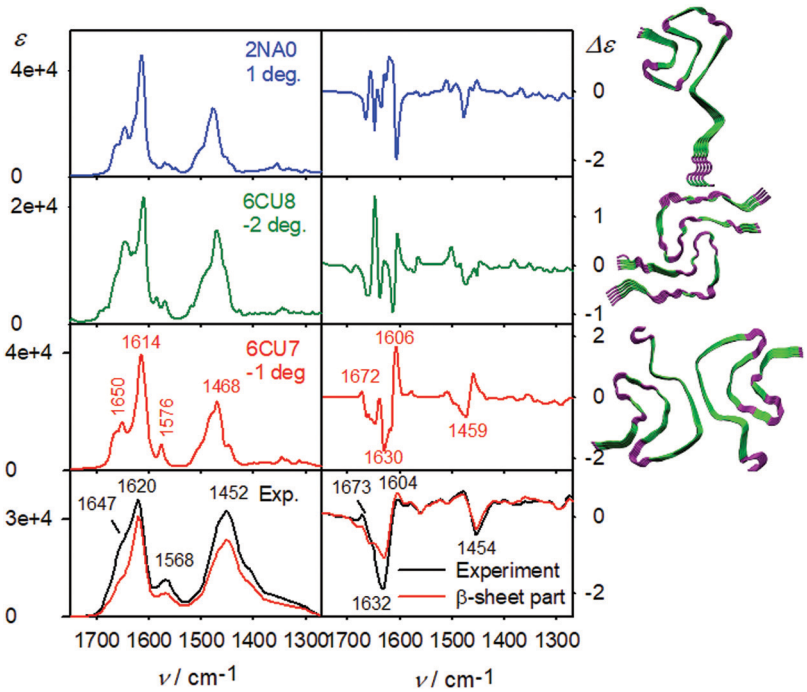

Fig. 5 IR and VCD spectra calculated for the three PDB αSyn fibril structures (2NA0, residues 34–97, 6CU8, res. 43–83, and 6CU7, res. 38–97) and the experimental spectra. In the calculation, 180 monomers were propagated in the periodic model, with the twist of neighboring protein chains indicated. For the experiment (in D_2O, bottom) a pure β-sheet contribution was estimated by partial (40%) subtraction of the spectrum of the disordered form and is plotted with the red line.

to be compatible with a two-strand 6CU7 fibril model and TEM imaging (Fig. 6, top). The twist might also differ locally. It affects fine band splitting observed in particular in VCD; IR and VCD spectra simulated for zero twist are plotted in Fig. S5 (ESI†).

Thus, although with some uncertainty, the VCD technique is able to distinguish the fine structure of αSyn fibrils in solution. However, we realize that the structure of ''our'' fibrils may not be identical to any of the three canonical structures suggested by the NMR and cryo-EM experiments. One has also to realize that a lower computational level has to be used than those for the monomeric forms (6-31G** instead of the 6-311++G** basis set, rigid idealized geometry instead of an MD average).

ROA spectra of fibrils exhibit polarization artifacts and effects inexplicable as vibrational ROA.[64,65] For αSyn, a strong background was present in the Raman spectrum, and also vibrational ROA bands were nearly hidden in the background signal. Some of the bands could be extracted, but the resemblance to the simulation was far from that allowing for a meaningful band to band comparison (Fig. S6, ESI†). Nevertheless, the specific scattering behavior suggests that the spectra can also be useful in the future, when we understand them better. Microscopy (TEM) images of the fibrils can be found in Fig. S7 (ESI†).

Conclusions

Using the Cartesian tensor transfer technique we showed that the spectra of vibrational optical activity can be clearly related to the αSyn secondary structure. In the disordered protein state the peptide backbone to a large extent adopts a polyproline II-like helix, which provides specific features in VCD and ROA spectra; so does the α-helical form. For the first time, a strong low-frequency (~50–200 cm^{-1}) ROA signal was observed and partially rationalized by the simulation. It can be used as an indicator of the PPII → α-helix transition, and was related to backbone and side chain motion. Also the ROA bands stemming from the C–H stretching motion significantly change with the αSyn conformation; for these bands, however, the measurement is difficult due to the low ROA to Raman intensity ratio, and spectra simulated at the harmonic level exhibit a large error. For the fibrils the idealized periodic model well reproduced basic features observed in the IR and VCD spectra. The fibrils also provided unique Raman and ROA signals, which, however, could not be fully interpreted in terms of vibrational optical activity. In spite of these drawbacks that will be addressed in the future we find the chiroptical spectroscopy coupled with spectral simulations extremely useful for monitoring of the protein and peptide folding. In particular, for αSyn and other amyloidogenic proteins, the methodology can contribute to the understanding and prevention of neurodegenerative diseases.

Conflicts of interest

There are no conflicts to declare.

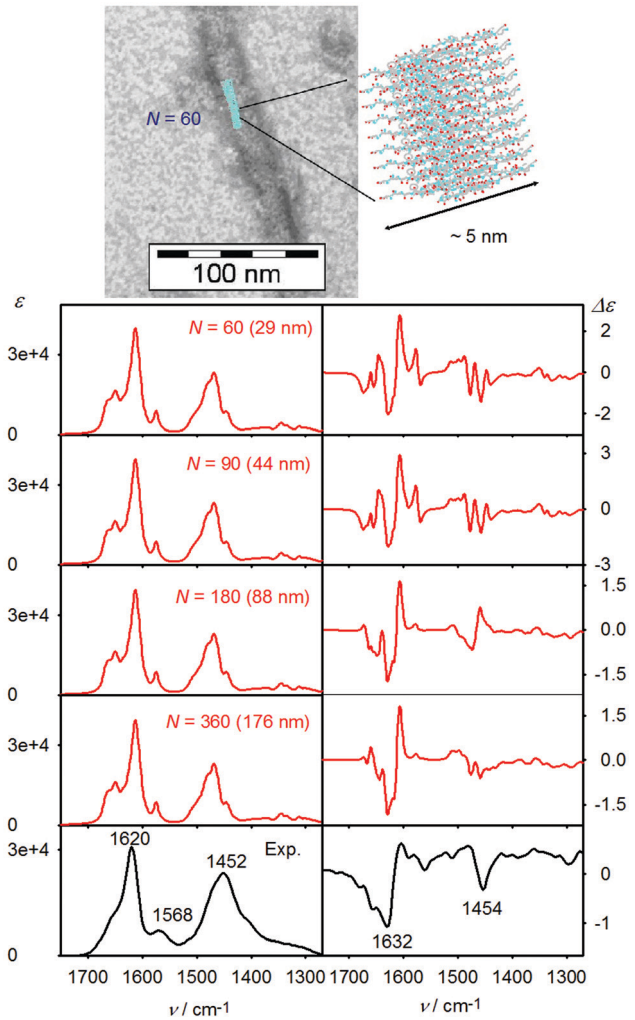

Fig. 6 IR and VCD spectra calculated for four fibril lengths and the experimental spectra. The number of αSyn molecules and approximate lengths are indicated; the 6CU7 geometry and −1° twist were used in the calculations. For the experiment, the spectrum obtained by a subtraction of the disordered part is shown. At the top, the N = 60 geometry is compared to a TEM image of the fibrils.

Acknowledgements

The work was supported by the Ministry of Education (CZ.02.1.01/0.0/0.0/16_019/0000729) and the Science Foundation (20-10144S) of the Czech Republic.

References

1 D. D. Murphy, S. M. Rueter, J. Q. Trojanowski and V. M.-Y. Lee, *J. Neurosci.*, 2000, **20**, 3214–3220.
2 W. S. Davidson, A. Jonas, D. F. Clayton and J. M. George, *J. Biol. Chem.*, 1998, **273**, 9443–9449.
3 P. H. Jensen, M. S. Nielsen, R. Jakes, C. G. Dotti and M. Goedert, *J. Biol. Chem.*, 1998, **273**, 26292–26294.
4 M. Baba, S. Nakajo, P. H. Tu, T. Tomita, K. Nakaya, V. M. Lee, J. Q. Trojanowski and T. Iwatsubo, *Am. J. Pathol.*, 1998, **152**, 879–884.
5 B. Li, P. Ge, K. A. Murray, P. Sheth, M. Zhang, G. Nair, M. R. Sawaya, W. S. Shin, D. R. Boyer, S. Ye, D. S. Eisenberg, Z. H. Zhou and L. Jiang, *Nat. Commun.*, 2018, **9**, 3609.
6 M. D. Tuttle, G. Comellas, A. J. Nieuwkoop, D. J. Covell, D. A. Berthold, K. D. Kloepper, J. M. Courtney, J. K. Kim, A. M. Barclay, A. Kendall, W. Wan, G. Stubbs, C. D. Schwieters, V. M. Y. Lee, J. M. George and C. M. Rienstra, *Nat. Struct. Mol. Biol.*, 2016, **23**, 409–415.
7 W. Peelaerts, L. Bousset, A. Van der Perren, A. Moskalyuk, R. Pulizzi, M. Giugliano, C. Van den Haute, R. Melki and V. Baekelandt, *Nature*, 2015, **522**, 340–344.
8 T. A. Keiderling, *Chem. Rev.*, 2020, **120**, 3381–3419.
9 R. K. Dukor and T. A. Keiderling, *Biopolymers*, 1991, **31**, 1747–1761.
10 S. Yamamoto, H. Watarai and P. Bouř, *Chem. Phys. Chem.*, 2011, **12**, 1509–1518.
11 S. Ma, X. Cao, M. Mak, A. Sadik, C. Walkner, T. B. Freedman, I. K. Lednev, R. K. Dukor and L. A. Nafie, *J. Am. Chem. Soc.*, 2007, **129**, 12364–12365.
12 C. D. Syme, E. W. Blanch, C. Holt, R. Jakes, M. Goedert, L. Hecht and L. D. Barron, *Eur. J. Biochem.*, 2002, **269**, 148–156.
13 C. Mensch, A. Konijnenberg, R. Van Elzen, A. M. Lambeir, F. Sobott and C. Johannessen, *J. Raman Spectrosc.*, 2017, **48**, 910–918.
14 E. Van de Vondel, P. Baatsen, R. Van Elzen, A. M. Lambeir, T. A. Keiderling, W. A. Herrebout and C. Johannessen, *Biochemistry*, 2018, **57**, 5989–5995.
15 B. Martial, T. Lefèvre, T. Buffeteau and M. Auger, *ACS Nano*, 2019, **13**, 3232–3242.
16 A. S. Kurochka, D. A. Yushchenko, P. Bouř and V. V. Shvadchak, *ACS Chem. Neurosci.*, 2021, **12**, 825–830.
17 A. Iyer, S. J. Roeters, V. Kogan, S. Woutersen, M. M. A. E. Claessens and V. Subramaniam, *J. Am. Chem. Soc.*, 2017, **139**, 15392–15400.
18 E. W. Blanch, I. H. McColl, L. Hecht, K. Nielsen and L. D. Barron, *Vib. Spectrosc.*, 2004, **35**, 87–92.
19 V. Baumruk, P. Pančoška and T. A. Keiderling, *J. Mol. Biol.*, 1996, **259**, 774–791.
20 G. Holzwarth and I. Chabay, *J. Chem. Phys.*, 1972, **57**, 1632–1635.
21 L. D. Barron and A. D. Buckingham, *J. Am. Chem. Soc.*, 1974, **96**, 4769–4773.
22 P. J. Stephens, *J. Phys. Chem.*, 1987, **91**, 1712–1715.
23 K. Ruud and J. Thorvaldsen, *Chirality*, 2009, **21**, E54–E67.
24 K. Ruud, T. Helgaker and P. Bouř, *J. Phys. Chem. A*, 2002, **106**, 7448–7455.
25 J. R. Cheeseman, M. J. Frisch, F. J. Devlin and P. J. Stephens, *Chem. Phys. Lett.*, 1996, **252**, 211–220.
26 P. Bouř and T. A. Keiderling, *J. Am. Chem. Soc.*, 1993, **115**, 9602–9607.
27 S. Luber and M. Reiher, *J. Phys. Chem. B*, 2010, **114**, 1057–1063.
28 S. Yamamoto, M. Straka, H. Watarai and P. Bouř, *Phys. Chem. Chem. Phys.*, 2010, **12**, 11021–11032.
29 K. V. J. Jose and K. Raghavachari, *Chirality*, 2016, **28**, 755–768.

 This journal is © the Owner Societies 2021

30 P. B. Karadakov and K. Morokuma, *Chem. Phys. Lett.*, 1987, **317**, 589–596.
31 P. Bouř, J. Sopková, L. Bednárová, P. Maloň and T. A. Keiderling, *J. Comput. Chem.*, 1997, **18**, 646–659.
32 S. Yamamoto, X. Li, K. Ruud and P. Bouř, *J. Chem. Theory Comput.*, 2012, **8**, 977–985.
33 N. S. Bieler, M. P. Haag, C. R. Jacob and M. Reiher, *J. Chem. Theory Comput.*, 2011, **7**, 1867–1881.
34 J. Kessler, V. Andrushchenko, J. Kapitán and P. Bouř, *Phys. Chem. Chem. Phys.*, 2018, **20**, 4926–4935.
35 J. Kessler, J. Kapitán and P. Bouř, *J. Phys. Chem. Lett.*, 2015, **6**, 3314–3319.
36 T. S. Ulmer, A. Bax, N. B. Cole and R. L. Nussbaum, *J. Biol. Chem.*, 2005, **280**, 9595–9603.
37 P. Gaur, M. Galkin, A. Kurochka, S. Ghosh, D. A. Yushchenko and V. V. Shvadchak, *ACS Chem. Neurosci.*, 2021, **12**, 1293–1298.
38 L. Nafie, *Vibrational optical activity: Principles and applications*, Wiley, Chichester, 2011.
39 P. Michal, R. Čelechovský, M. Dudka, J. Kapitán, M. Vůjtek, M. Berešová, J. Šebestík, K. Thangavel and P. Bouř, *J. Phys. Chem. B*, 2019, **123**, 2147–2156.
40 S. H. Lim, I. V. Peshenko, E. V. Olshevskaya, A. M. Dizhoor and J. B. Ames, *J. Biol. Chem.*, 2016, **291**, 4429–4441.
41 T. E. Creighton, *Proteins: Structures and Molecular Properties*, W. H. Freeman and Co., New York, 2nd edn, 1993.
42 D. A. Case, I. T. E. Cheatham, T. Darden, H. Gohlke, R. Luo, J. K. M. Merz, A. Onufriev, C. Simmerling, B. Wang and R. Woods, *J. Comput. Chem.*, 2005, **26**, 1668–1688.
43 J. Wang, P. Cieplak and P. A. Kollman, *J. Comput. Chem.*, 2000, **21**, 1049–1074.
44 W. L. Jorgensen, J. Chandrasekhar and J. D. Madura, *J. Chem. Phys.*, 1983, **79**, 926–935.
45 P. Bouř and T. A. Keiderling, *J. Chem. Phys.*, 2002, **117**, 4126–4132.
46 J. Hudecová, K. H. Hopmann and P. Bouř, *J. Phys. Chem. B*, 2012, **116**, 336–342.
47 P. Bouř, *CCT, Program for Cartesian tensor transfer*, Academy of Sciences, Prague, 1997–2019.
48 M. J. Frisch, G. W. Trucks, H. B. Schlegel, G. E. Scuseria, M. A. Robb, J. R. Cheeseman, G. Scalmani, V. Barone, G. A. Petersson, H. Nakatsuji, X. Li, M. Caricato, A. V. Marenich, J. Bloino, B. G. Janesko, R. Gomperts, B. Mennucci, H. P. Hratchian, J. V. Ortiz, A. F. Izmaylov, J. L. Sonnenberg, D. Williams-Young, F. Ding, F. Lipparini, F. Egidi, J. Goings, B. Peng, A. Petrone, T. Henderson, D. Ranasinghe, V. G. Zakrzewski, J. Gao, N. Rega, G. Zheng, W. Liang, M. Hada, M. Ehara, K. Toyota, R. Fukuda, J. Hasegawa, M. Ishida, T. Nakajima, Y. Honda, O. Kitao, H. Nakai, T. Vreven, K. Throssell, J. A. Montgomery Jr., J. E. Peralta, F. Ogliaro, M. J. Bearpark, J. J. Heyd, E. N. Brothers, K. N. Kudin, V. N. Staroverov, T. A. Keith, R. Kobayashi, J. Normand, K. Raghavachari, A. P. Rendell, J. C. Burant, S. S. Iyengar, J. Tomasi, M. Cossi, J. M. Millam, M. Klene, C. Adamo, R. Cammi, J. W. Ochterski, R. L. Martin, K. Morokuma, O. Farkas, J. B. Foresman and D. J. Fox, *Gaussian 16 Rev. A.03*, Gaussian, Inc., Wallingford, CT, 2016.
49 J. P. Perdew, K. Burke and Y. Wang, *Phys. Rev. B: Condens. Matter Mater. Phys.*, 1996, **54**, 16533–16539.
50 Y. Takano and K. N. Houk, *J. Chem. Theory Comput.*, 2005, **1**, 70–77.
51 L. D. Barron, *Molecular Light Scattering and Optical Activity*, Cambridge University Press, Cambridge, UK, 2004.
52 J. Kubelka and T. A. Keiderling, *J. Phys. Chem. A*, 2001, **105**, 10922–10928.
53 P. Bouř and T. A. Keiderling, *J. Chem. Phys.*, 2003, **119**, 11253–11262.
54 L. Piseri and G. Zerbi, *J. Mol. Spectrosc.*, 1968, **26**, 254–261.
55 P. K. Misra, *Physics of condensed matter*, Elsevier, San Diego, USA, 2012.
56 J. Průša and P. Bouř, *Chirality*, 2018, **30**, 55–64.
57 T. Measey and R. Schweitzer-Stenner, *J. Am. Chem. Soc.*, 2011, **133**, 1066–1076.
58 J. Kubelka, J. Kim, P. Bouř and T. A. Keiderling, *Vib. Spectrosc.*, 2006, **42**, 63–73.
59 F. J. Zhu, N. W. Isaacs, L. Hecht and L. D. Barron, *Structure*, 2005, **13**, 1409–1419.
60 V. Palivec, P. Michal, J. Kapitán, H. Martinez-Seara and P. Bouř, *Chem. Phys. Chem.*, 2020, **21**, 1272–1279.
61 A. Fulara, A. Lakhani, S. Wójcik, H. Nieznańska, T. A. Keiderling and W. Dzwolak, *J. Phys. Chem. B*, 2011, **115**, 11010–11016.
62 R. Huang, V. Setnička, M. A. Etienne, J. Kim, J. Kubelka, R. P. Hammer and T. A. Keiderling, *J. Am. Chem. Soc.*, 2007, **129**, 13592–13603.
63 M. Krupová, J. Kessler and P. Bouř, *Chem. Phys. Chem.*, 2021, **22**, 83–91.
64 M. Krupová, J. Kessler and P. Bouř, *ChemPlusChem*, 2020, **85**, 561–575.
65 S. Yamamoto and H. Watarai, *Chirality*, 2012, **24**, 97–103.